9872 *Macromolecules* **2004,** *37,* 9872−9879

Surface-Constrained Foaming of Polymer Thin Films with Supercritical Carbon Dioxide

Srinivas Siripurapu,[†,§] **John A. Coughlan,**[†] **Richard J. Spontak,**[†,‡] **and Saad A. Khan***[,†]

Departments of Chemical & Biomolecular Engineering and Materials Science & Engineering, North Carolina State University, Raleigh, North Carolina 27695

Received July 22, 2004; Revised Manuscript Received October 8, 2004

ABSTRACT: Microcellular polymer foams afford a wide variety of attributes relative to their dense analogues, and efforts remain underway to establish viable routes to generate foams with substantially reduced pore cell size and increased pore cell density. Barrier constraints are applied in the present work to achieve diffusion-controlled isothermal foaming of thin polymer films in the presence of supercritical carbon dioxide (scCO$_2$). Poly(methyl methacrylate) (PMMA) films measuring ca. 95−100 μm in thickness are physically constrained between two impenetrable plates so that scCO$_2$ exit diffusion is restricted to the film edges. Results obtained here demonstrate that the pore size can be systematically reduced to less than 100 nm in such systems by applying high saturation scCO$_2$ pressures, relatively low foaming temperatures (near the glass transition temperature of the scCO$_2$-plasticized polymer), and a rapid pressure quench. Classical nucleation theory (CNT) modified to account for the compressible nature of scCO$_2$ is used to describe pore cell growth as a function of foaming temperature and scCO$_2$ saturation pressure. Incorporation of a gradient model based on the Sanchez−Lacombe equation of state to account for PMMA−CO$_2$ interfacial tension in conjunction with the CNT yields accurate predictions of foam cell densities as a function of relevant system parameters.

Introduction

Supercritical CO$_2$ (scCO$_2$) is a versatile compressible solvent that can be used to facilitate numerous polymer processes.[1−3] In addition to being environmentally benign, naturally abundant, and relatively inexpensive,[4−6] scCO$_2$ has attracted much attention as a physical blowing agent for use in polymer foaming, since its tunable properties can provide exceptional control of foam morphologies through systematic variation of scCO$_2$ pressure (or, equivalently, density) under isothermal conditions. In the past decade, continuous[7−9] and batch[10−16] foaming methodologies have been developed to generate well-defined microcellular foams with cell diameters measuring on the order of 10 μm or less from glassy polymers in the presence of scCO$_2$. Pressure-induced foaming is conducted according to the following process sequence: a homogeneous polymer/gas solution prepared at high pressure is subjected to a rapid pressure quench to promote the nucleation of gas bubbles, which subsequently grow until the temperature of the heterogeneous solution drops below the glass transition temperature (T_g) of the plasticized polymer and the pore cells become immobilized within the vitrified polymer matrix.

Prior polymer foaming studies have employed scCO$_2$ as a porogen for glassy thermoplastics such as polystyrene,[8,12,13] polycarbonate,[11] polysulfone,[14] poly(methyl methacrylate) (PMMA),[16] and polyimide[15] as well as for a few semicrystalline thermoplastics, e.g., poly(ethylene terephthalate)[17] and polyamide.[18] The foamed structures may exhibit either wholly closed or open pore cells, or a mixture thereof, depending on the processing conditions and physical properties of the polymer. Closed cell foams are particularly beneficial in technologies requiring lightweight barrier or high-strength materials[19−21] whereas open cell foams are useful as separations membranes, fuel cells, tissue scaffolds, and drug-release substrates.[22−26] Most foaming studies performed to date have focused on (i) discerning the *foamability* of a given bulk polymer and (ii) tailoring the final foam morphology through systematic variation of saturation pressure, exposure time, foaming temperature, and depressurization rate. To relate some of these variables, Krause et al.[14] have introduced the concept of a "foam diagram," which identifies the existence of the critical scCO$_2$ concentration required to switch from closed- to open-cell morphologies.

Development of porous polymer thin films has become increasingly important due to the number of emergent technologies based on such materials.[23,27−32] This is typically achieved through extensive use of organic solvents in multiple steps. In contrast, the use of scCO$_2$ as a porogen to generate nanoporous polymer films without postpurification appears highly attractive. Recent results reported by Krause et al.[33] confirm the formation of open-cell nanoporous morphologies in polysulfone/polyimide blends subjected to scCO$_2$ foaming. In this work, we introduce a novel protocol by which PMMA thin films are foamed by isothermal pressure-induced phase separation in the presence of scCO$_2$ over a wide range of operating conditions. Results obtained during this study demonstrate that, by constraining CO$_2$ surface diffusion through the use of impenetrable barriers positioned on each side of the polymer film, uniform foam morphologies with high cell densities can be routinely produced. Such surface-mediated homogeneous nucleation is examined in the context of classical nucleation theory (CNT) modified accordingly to account

---

[†] Department of Chemical & Biomolecular Engineering.

[‡] Department of Materials Science & Engineering.

[§] Present address: GE Advanced Materials, 1 Lexan Lane, Mt. Vernon, IN 47620.

[*] To whom correspondence should be addressed: e-mail khan@eos.ncsu.edu.

10.1021/ma0484983 CCC: $27.50

for $scCO_2$ as the porogen, and predicted pore cell densities are found to compare favorably with experimental results.

Theoretical Background

The mechanism of microcellular foaming in polymers has been generally described by homogeneous classical nucleation models,[34–36] although new theoretical developments have been introduced to provide a more rigorous thermodynamic interpretation of the nucleation process.[37] In the present work, we extend the CNT, which embodies the essential physics of nucleation, to $scCO_2$-induced foaming of polymer films by accounting for the effect of $scCO_2$ compressibility on surface tension. In the framework of CNT, the rate of homogeneous nucleation is given by[36]

$$N_{\mathrm{h}} = Cf \exp\left(-\frac{\Delta G_{\mathrm{h}}}{kT}\right) \qquad (1)$$

where N_{h} is the rate at which the number of bubble nuclei is generated per unit volume, C is the porogen density, f is the frequency factor of porogen molecules, k is the Boltzmann constant, and T denotes absolute temperature. The energy barrier for homogeneous nucleation (ΔG_{h}) is[36]

$$\Delta G_{\mathrm{h}} = \frac{16\pi\gamma_{\mathrm{bp}}^{3}}{3\Delta P^{3}} \qquad (2)$$

where ΔP is the magnitude of the pressure quench and γ_{bp} is the interfacial tension at the polymer–$scCO_2$ interface.

The interfacial tension can be represented by combining the Cahn–Hilliard gradient model and a suitable equation of state[38] such as the Sanchez–Lacombe[39] lattice-fluid equation of state, which likewise predicts density and composition as functions of pressure and temperature, viz.,

$$\tilde{\rho}^2 + \tilde{P} + \tilde{T}\left[\ln(1-\tilde{\rho}) + \left(1 - \frac{1}{r}\right)\tilde{\rho}\right] = 0 \qquad (3)$$

where r is the number of occupied lattice sites, and $\tilde{\rho}$, $\tilde{P}$, and $\tilde{T}$ represent reduced density, pressure, and temperature, respectively. A detailed discussion of this equation of state with respect to polymer–$scCO_2$ systems is available elsewhere.[40] In the case of a phase-separated binary polymer–$scCO_2$ system, the interfacial tension can be expressed as[38]

$$\gamma_{\mathrm{bp}} = 2^{1/2}\,\frac{|[\kappa_{11}^{1/2} + \kappa_{22}^{1/2}(\Delta\rho_2/\Delta\rho_1)]|}{v_{\mathrm{m},1}^{*}} \int_{\phi_1^{\mathrm{I}}}^{\phi_1^{\mathrm{II}}} \tilde{\rho}\,\Delta a^{1/2}\,\mathrm{d}\phi_1 \qquad (4)$$

Here, $\Delta\rho_i$ is the density difference of component i ($i = 1$ or 2) partitioned between two coexisting phases (denoted by I and II), $\tilde{\rho}$ is the reduced density, ϕ_i is the volume fraction of species i, κ_{ij} is an interaction parameter between species i and j, and $v_{\mathrm{m},i}^{*}$ is the unit volume of species i. The change in interfacial free energy density (Δa) is the difference between the actual interfacial free energy density and that which would exist if a line of zero thickness separated each phase, i.e.

$$\Delta a = \tilde{\rho}\left[g - \left(\frac{\phi_1}{v_{\mathrm{m},1}^{*}}\right)\mu_1^{\mathrm{e}} - \left(\frac{\phi_2}{v_{\mathrm{m},2}^{*}}\right)\mu_2^{\mathrm{e}}\right] \qquad (5)$$

where μ_i^{e} is the equilibrium chemical potential of component i. The term g signifies the molar Gibbs free energy of a homogeneous interfacial region:

$$g = -\tilde{\rho}P^{*} + P/\tilde{\rho} + kT\left[\frac{(1/\tilde{\rho} - 1)\ln(1-\tilde{\rho})}{v_0^{*}} + \frac{\ln\tilde{\rho}}{v^{*}} + \frac{\phi_1 \ln \phi_1}{v_1^{*}} + \frac{\phi_2 \ln\phi_2}{v_2^{*}}\right] \qquad (6)$$

Combining eqs 4–6, followed by numerical integration in combination with appropriate mixing rules for the interfacial region (provided with the Sanchez–Lacombe[39] equation of state), yields predictions for PMMA–$scCO_2$ interfacial tension in terms of system temperature and pressure.

The frequency factor of porogen molecules (f) can be written[27] as $4\pi r_{\mathrm{c}}^{3}ZR_{\mathrm{imp}}$, where Z is the Zeldovich factor that accounts for cell coalescence, R_{imp} is the rate of impingement of gas molecules per unit area, and r_{c} is the critical nucleus radius given by $2\gamma_{\mathrm{bp}}/\Delta P$. It immediately follows that the theoretical cell density N_{th} can be ascertained from

$$N_{\mathrm{th}} = \int_{P_{\mathrm{sat}}}^{P_{\mathrm{atm}}} N_{\mathrm{h}}\,\frac{\mathrm{d}P}{\mathrm{d}P/\mathrm{d}t} \qquad (7)$$

where P_{sat} is the saturation pressure of the blowing agent, P_{atm} is atmospheric pressure, and $\mathrm{d}P/\mathrm{d}t$ represents the depressurization (vent) rate. Equations 1–7 constitute the complete framework for the modified CNT proposed here. Within the context of this framework, the term ZR_{imp} serves as a one-time fitted parameter, while pure-component properties are obtained from tabulated sources. The density of the polymer–$scCO_2$ mixture is combined with the composition of the mixture (both computed from the Sanchez–Lacombe[39] equation of state) to yield the temperature- and pressure-dependent porogen concentration (C) in the swollen polymer network. Thus, values of N_{th} are predicted in terms of temperature, pressure, and depressurization rate for any polymer–$scCO_2$ system insofar as the polymer is molten and pure-component properties are available.

Experimental Section

Materials. The PMMA (Plexiglas VM-100) employed in this study was provided in pellet form by Elf Atofina N.A. (King of Prussia, PA) and purified prior to foaming. The number- and weight-average molecular weights from GPC analysis of the purified PMMA were 70 000 and 107 000, respectively, and the mass density at 25 °C was 1.18 g/cm^3. Carbon dioxide (>99.8% pure) was obtained from National Specialty Gases (Durham, NC), whereas reagent-grade toluene (99.98% pure) was purchased from Aldrich Chemicals (St. Louis, MO) and used as-received.

Methods. A 10 wt % solution of PMMA in toluene was prepared by dissolving the polymer for 12 h and subsequently filtered using 0.45 μm membranes. Pure PMMA was precipitated from the solution and redissolved in toluene at a concentration of 30 wt % PMMA. Thin films measuring 95–100 μm thick were produced by casting this solution on a glass plate with a universal blade applicator (Gardco Corp., Miami, FL). The cast films were dried for 48 h at ambient temperature and then placed under vacuum at 40 °C for another 24 h. Densified PMMA films were removed from the glass plate by immersing the plate in water, and free-standing films were subjected to vacuum-drying at 40 °C for an additional 12 h to remove residual water or solvent prior to foaming. The batch foaming assembly, schematically depicted in Figure 1, consisted of a high-pressure view cell that housed the polymer

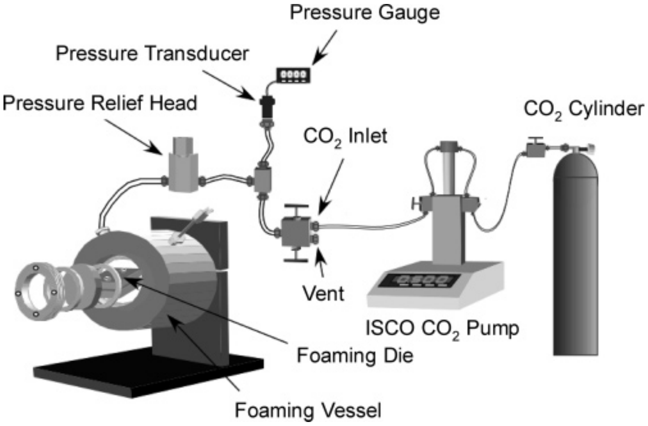

Figure 1. Schematic diagram illustrating the setup employed in this work to foam polymer thin films in the presence of surface constraints to control scCO$_2$ diffusion upon depressurization.

films. The films were either sandwiched in a foaming die (explained later) or left free-standing. The entire cell was placed in an oven with a cascade control of heating and cooling elements to ensure uniform temperature distribution within ±0.5 °C. Gaseous CO$_2$ was fed to the cell from an ISCO high-pressure pump at a fixed pressure. Desired pressure and temperature conditions were accurately maintained by a Bridgeview process control algorithm in conjunction with a Fieldpoint data acquisition system. The interfaced control valve assembly in this configuration also permitted systematic variation of dP/dt to alter the rate of bubble nucleation. The dried polymer films were cut into 1.3 cm × 2.5 cm rectangles for foaming experiments. Once the cell was heated to a desired foaming temperature, each specimen was saturated with scCO$_2$ for a desired period of time (6 h was found to be sufficient) at an elevated pressure up to 34.5 MPa. After this time, the foaming cell was depressurized rapidly under isothermal conditions to promote pressure-induced phase separation of scCO$_2$ from the PMMA to yield the final foam.

Foamed samples were dried under vacuum at 50 °C for 24 h, fractured in liquid nitrogen, and mounted on stubs with carbon tape for Au/Pd sputtering in an Anatech Hummer 5 sputtering system. Films prepared for secondary electron imaging were pulse-coated with 25 nm of Au/Pd, dried under vacuum for an additional 24 h, and examined by scanning electron microscopy (SEM) with a Philips 505T electron microscope. Select uncoated specimens were imaged with backscattered electrons in a variable-pressure Hitachi S3200N electron microscope maintained at a chamber pressure of 60 Pa of He. Images were acquired at an accelerating voltage of 10−15 kV. Secondary electron images were analyzed for cell diameters, cell densities, and the thickness of the unfoamed outer skin. The cell diameter was taken as the average of two orthogonal cell dimensions, and the cell density was calculated using the method of Kumar and Suh.[10]

Results and Discussion

Our attempt to foam thin polymer films using principles established for bulk polymers[19−21] is illustrated in Figure 2, which shows an image acquired from a PMMA film foamed in scCO$_2$ at 31.0 MPa and 50 °C. The foam clearly exhibits three distinct regions: (i) a microcellular core, (ii) a transition zone between the core and unfoamed skin, and (iii) a relatively thick unfoamed surface skin accounting for almost 70% of the film thickness. The microcellular core possesses a mean cell diameter of ca. 1 μm and a cell density of ca. 10^{11} cells/cm^3. Attempts to improve the foaming process (i.e., reduce cell size, increase cell density, and decrease skin thickness) by varying temperature and pressure do not substantially improve the ultimate foam morphology.

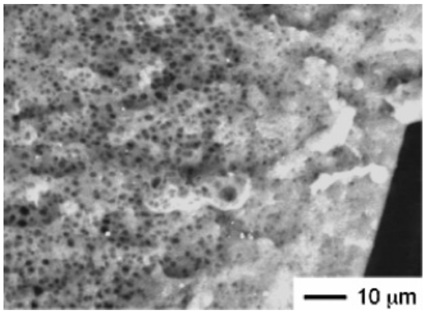

Figure 2. Backscattered SEM image of a PMMA film foamed at 50 °C and 31.0 MPa scCO$_2$ after an exposure time of 6 h and a depressurization rate of 6.89 MPa/s without diffusion control.

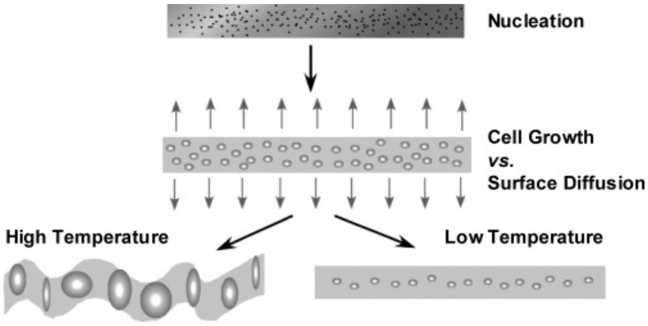

Figure 3. Illustration depicting the outcome of foaming thin polymer films at different temperatures in the absence of surface constraints. At high temperatures, large, polydisperse cells form and reshape the polymer film. At low temperatures, small cells form within the film core, resulting in thick, nonporous ("skin") regions near the film surfaces.

Diffusion-Controlled Foaming. The results displayed in Figure 2 can be understood by recognizing the underlying differences between foaming bulk polymers and thin polymer films. An illustration of the foaming process in thin polymer films is provided in Figure 3. Each step in the sequence of events described earlier for pressure-induced foaming is crucial to the development of the final foam morphology and relates back to CNT. The formation of discrete CO$_2$ bubbles induced by a sudden change in the pressure of the supersaturated PMMA−scCO$_2$ solution proceeds by nucleation. When a CO$_2$ nucleus forms, its spherical shape minimizes the interfacial energy between the CO$_2$-rich nucleus and the higher-viscosity molten polymer matrix. As the solubility of CO$_2$ in the polymer decreases and more CO$_2$ molecules separate from the solution, three possibilities arise. If, in scenario I, the degree of supersaturation is sufficiently high so that ΔG_{h} in eqs 1 and 2 is overcome, new stable nuclei develop. In the absence of such supersaturation (scenario II), CO$_2$ molecules diffuse into preexisting bubbles, thereby causing them to grow. Scenario III witnesses the migration of CO$_2$ molecules to external surfaces where they exit the polymer matrix. These three processes are competitive and depend on factors such as the quantity of CO$_2$ molecules available for nucleation, the rate at which CO$_2$ is available, the physical characteristics of the polymer-rich phase, and the interactions between the two phases. The CO$_2$ bubbles ultimately generated must be stabilized as the polymer-rich phase vitrifies to form a final foam morphology.

Foaming polymer thin films introduces a fundamental dilemma: CO$_2$ diffusion from the film surfaces occurs on a comparable time scale as pore cell growth. Because

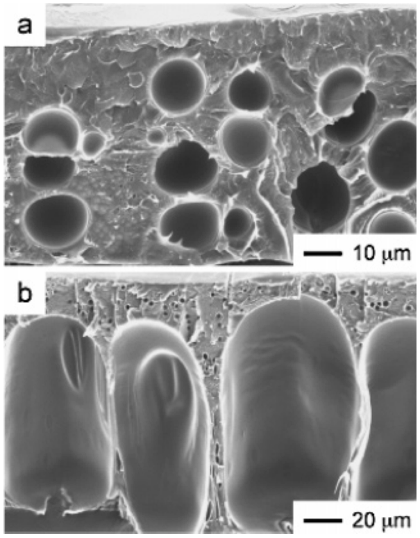

Figure 4. SEM images of PMMA films foamed at 34.5 MPa $scCO_2$ after an exposure time of 6 h and a depressurization rate of 6.89 MPa/s without surface constraints at two temperatures (in °C): (a) 40 and (b) 80. These experimental results confirm the illustration displayed in Figure 3.

of the relatively large area available for CO_2 molecules to exit the swollen polymer, the CO_2 reservoir required for additional nucleation and cell growth (intrinsically limited due to the mass of the film) is rapidly depleted. These two opposing transport mechanisms—surface diffusion and pore cell growth—are responsible for variable material properties (e.g., viscosity, T_g, and diffusion coefficients) along the surface normal. Such heterogeneity, combined with variable processing conditions (such as differences in temperature, as shown in Figure 3), yields nonuniform foam morphologies. High-temperature foaming promotes the formation of large, polydisperse cells and an irregular skin thickness with discontinuous surfaces. At lower temperatures (closer to the T_g of the polymer−gas solution), foams possess a relatively uniform microcellular core and a smooth contiguous skin (cf. Figure 2). The SEM images presented in Figure 4 show PMMA thin films foamed at two temperatures (80 °C in Figure 4a and 40 °C in Figure 4b) under isobaric conditions (34.5 MPa) and exemplify the two regimes portrayed in Figure 3. More detailed descriptions of foaming conditions will be provided in later sections.

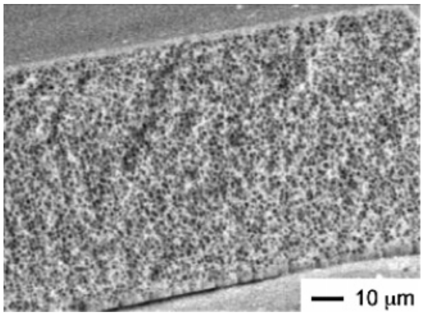

Figure 5. Backscattered SEM image of a PMMA film foamed at 50 °C and 31.0 MPa $scCO_2$ after an exposure time of 6 h and a depressurization rate of 6.89 MPa/s with surface constraints. Compare these results with those provided in Figure 2.

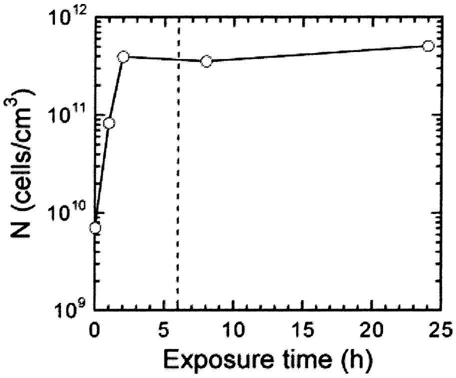

Figure 6. Dependence of cell density (N) on exposure time at 40 °C and 34.5 MPa $scCO_2$ after a depressurization rate of 6.89 MPa/s with surface constraints. The solid line connects the data, and the vertical line identifies the exposure time used throughout the remainder of this study.

In light of these observations, restricting CO_2 surface diffusion is anticipated to increase the availability of CO_2 for cell nucleation and growth as well as for enhanced cell uniformity. To test this hypothesis, a metal foaming die has been designed and machined with smooth planar surfaces which, when used to sandwich the polymer thin film, serves as a physical barrier to CO_2 diffusion from the film surfaces. During depressurization, CO_2 molecules may only escape from the film through the relatively thin edges, thereby increasing the residence time of CO_2 within the CO_2-swollen polymer. Figure 5 shows a micrograph of a PMMA film foamed under identical conditions as the one displayed in Figure 2, but with the surface constraint. The difference in foam morphology is obvious. Distinguishing characteristics of the surface-constrained foam are cell uniformity and an ultrathin layer (corresponding to a single layer of cells) of unfoamed skin with a smooth surface. Confinement of the thin film in the foaming die appears to eliminate property gradients across the film thickness, as well as promote uniform cell growth, thereby yielding a fully microcellular foamed film. In the following sections, the roles played by several process variables in foaming constrained polymer thin films have been systematically investigated to elucidate the mechanism of foaming polymer thin films and test theoretical predictions.

Effect of Exposure Time. To understand the dependence of cell density on process variables, we must first ensure that the time of exposure is sufficient for $scCO_2$ sorption into the polymer to reach its thermodynamic solubility. Diffusion-regulated foaming has been performed at a constant temperature of 40 °C and a $scCO_2$ saturation pressure of 34.5 MPa for exposure times ranging from 15 min to 24 h. Measured cell densities (N) are provided as a function of exposure time in Figure 6 and confirm that CO_2 sorption reaches its equilibrium solubility after about 2 h. Although it was not measured here, the saturation time of $scCO_2$ in analogous unconstrained polymer thin films is expected to be substantially shorter due to the greater surface area available for sorption. In marked contrast, the saturation time measured[10] from bulk foaming studies of thick PMMA disks is ~22 h. This difference in saturation times is attributed to the diffusion path length, which scales as $time^{1/2}$ if we assume that (i) the concentration-average diffusion coefficient depends only on temperature and (ii) pressure and edge effects are negligible. By extrapolation, the saturation time for an *unconstrained* PMMA film measuring 100 μm thick is estimated to be only ~3 min, which illustrates the impact of surface barriers on CO_2 diffusion. On the basis

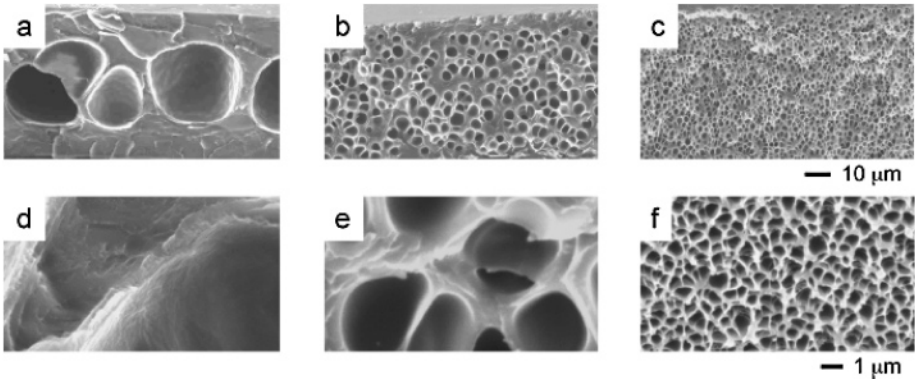

Figure 7. SEM images of PMMA films foamed at 40 °C and a depressurization rate of 6.89/s with surface constraints at three $scCO_2$ pressures (in MPa): (a) 6.89, (b) 17.2, and (c) 34.5. The images in the bottom row are enlargements of the corresponding images in the top row.

of these observations, we have elected to use a constant exposure time of 6 h throughout the remainder of this study.

Effect of Saturation Pressure. Figure 7 shows a series of SEM images acquired from foam morphologies generated after pressure quenches conducted at 40 °C and 6.89 MPa/s from 6.89 to 34.5 MPa $scCO_2$. All the foams exhibit a uniform cell morphology and a dense (unfoamed) skin, the thickness of which depends on the saturation pressure. While no foaming is observed at lower pressures (e.g., 5.52 MPa), bubble nucleation is evident at 6.89 MPa, which is close to the critical pressure of CO_2 (7.38 MPa). A sharp increase in cell density by over 3 orders of magnitude occurs at 10.3 MPa. This transition differs from results reported[10] for bulk PMMA foamed with $scCO_2$, wherein high levels of cell nucleation ($\sim 10^{11}$ cells/cm^3) are only achieved at saturation pressures in excess of 27.6 MPa. The enlargements included in Figure 7 more clearly reveal the fine differences in pore cell size and shape that accompany the increase in saturation pressure. Since the saturation pressure is a measure of the amount of $scCO_2$ available for cell nucleation and growth, a low saturation pressure translates into a limited $scCO_2$ reservoir. This relationship is consistent with the foam morphologies, composed of isolated and spherical pore cells, generated at low pressures. As the $scCO_2$ pressure is increased (and the amount and rate at which CO_2 molecules become available for nucleation likewise increase), a larger population of cells is capable of rapid nucleation.

As the pore cells grow, the foam expands, and the molten polymer-rich phase between neighboring cells thins. Continued cell growth reduces the intercellular distance so that the pore cells eventually lose their spherical shape and adopt a close packing arrangement that is the most energetically favorable at the time of polymer vitrification. The foam morphology produced at 34.5 MPa (Figure 7c,f) consists of fine pore cells separated by thin flat struts. Foaming constrained PMMA thin films under the operating conditions listed above yields pore cells with diameters commonly ranging from <100 to ~400 nm. Figure 7c, in particular, confirms the existence of a *closed*-cell porous morphology. This observation is contrary to results from independent studies[15,33] reporting the formation of a bicontinuous *open*-cell nanoporous morphology in polysulfone and poly(ether imide) at high $scCO_2$ concentrations. Pore cell densities and sizes extracted from images such as those presented in Figure 7 are displayed as functions of CO_2 pressure in parts a and b, respectively of Figure 8. Variation in $scCO_2$ pressure is responsible for pore cell densities that vary by as much as 4 orders of magnitude. Similarly, average cell sizes range from 30 μm to <200 nm as the concentration of $scCO_2$ is increased under isothermal conditions.

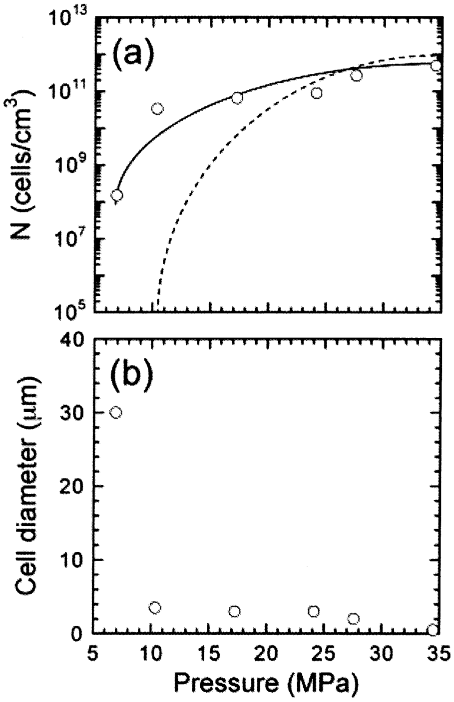

Figure 8. Cell density (a) and average cell diameter (b) as functions of $scCO_2$ pressure at 40 °C and a depressurization rate of 6.89 MPa/s with surface constraints. Solid and dashed lines in (a) are predictions from the modified nucleation theory proposed here and CNT, respectively.

Two other noteworthy characteristics warrant discussion at this juncture. The first is the thickness of the unfoamed skin, which appears to measure on the same length scale as a single layer of pore cells at each operating pressure examined and therefore varies accordingly. The second is the rapid increase in pore cell density with increasing CO_2 pressure between 6.89 and 13.8 MPa. This trend is accurately captured in predictions from the modified CNT. The solid line included in Figure 8a denotes the predicted effect of $scCO_2$ pressure on pore cell density of the foamed films and demonstrates excellent agreement between predictions from the present theoretical framework and experimental observations, especially at high pressures (since

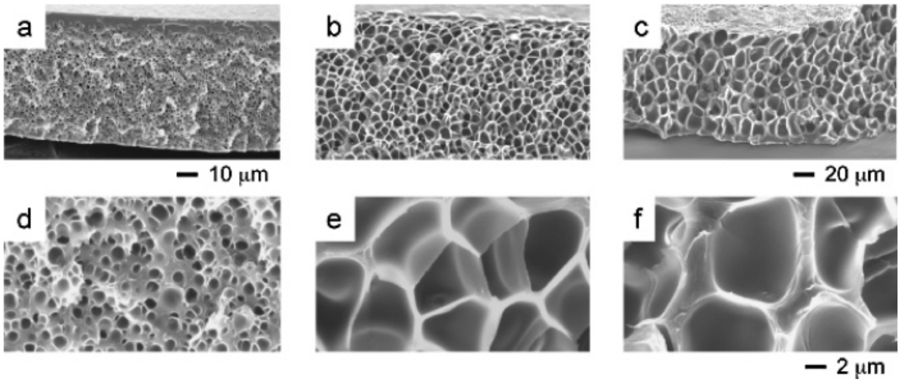

Figure 9. SEM images of PMMA films foamed at 34.5 MPa $scCO_2$ and a depressurization rate of 6.89 MPa/s with surface constraints at three temperatures (in °C): (a) 35, (b) 80, and (c) 120. The images in the bottom row have the same magnification and are enlargements of the corresponding images in the top row. Note the magnification change in (a) in the top row from those in (b) and (c).

the polymer−CO_2 solution is liquidlike at these conditions). The Sanchez−Lacombe[39] equation of state, as well as the interfacial tension expressions employed here, offers accurate predictions for homogeneous nucleation in polymers foamed with high-pressure CO_2.

Effect of Temperature. The foaming temperature constitutes another important design consideration, since the extent of foaming, commonly expressed in terms of pore cell size, is dictated by how far the polymer−CO_2 solution is removed from its T_g. For this reason, the foaming temperature in the present study has been varied from 25 °C, which is just below the critical temperature of CO_2 (31.1 °C), to 120 °C at 34.5 MPa and a depressurization rate of 6.89 MPa/s. The SEM images presented in Figure 9 illustrate foamed morphologies generated at three different temperatures, and the corresponding cell densities and mean cell diameters are provided as functions of temperature in parts a and b, respectively of Figure 10. No foaming is observed at the lowest temperature. Previous efforts by Goel and Beckman[11] have shown that the T_g of PMMA can drop to as low as 32 °C when exposed to high $scCO_2$ pressures. Foaming first occurs here when the temperature is increased to 35 °C, and cell densities exhibit a maximum in the vicinity of 40 °C (Zone I in Figure 10a) before decreasing with increasing temperature (and decreasing polymer melt strength[8]) up to 120 °C (Zone II). Similar variation in pore cell density has been reported by Krause et al.[14] in their efforts to foam high-T_g polymers.

A profound difference is apparent in the pore cell morphologies generated within these two temperature zones. At the lowest foaming temperature, tiny spherical cells are surrounded by relatively thick cell walls. This morphology reflects the leathery (high-viscosity) nature of plasticized PMMA not far removed from its T_g during foaming. At temperatures higher than the T_g of the solution (>40 °C), a large population of pore cells exhibits uniform size and shape with relatively thin cell walls. At very high temperatures, however, the cells are distorted due to the high rate of cell coalescence and long growth time afforded by the low polymer viscosity prior to vitrification. Pore cell densities predicted from the modified CNT framework developed here are included in Figure 10a and exhibit reasonably good agreement with the experimental data. While the predictions indicate that the pore cell density decreases with increasing temperature in Zone II, they become increasingly less accurate at low temperatures in Zone I. Recall that, in this zone, the plasticized PMMA behaves as a viscoelastic solid and not as a molten polymer, which is expected to introduce errors in the Sanchez−Lacombe[39] equation of state.

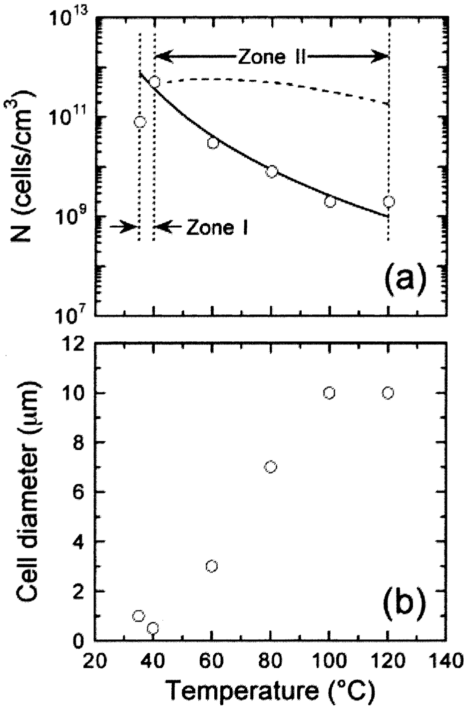

Figure 10. Cell density (a) and average cell diameter (b) presented as functions of temperature at 34.5 MPa $scCO_2$ and a depressurization rate of 6.89 MPa/s with surface constraints. Solid and dashed lines in (a) are predictions from the modified nucleation theory proposed here and CNT, respectively. The two zone designations are discussed in the text.

Effect of Depressurization Rate. The depressurization rate limits the rate at which CO_2 is available for cell growth upon phase separation and thus represents the driving force for cell evolution. As such, the pore cell density is expected to increase with increasing depressurization rate. To test this hypothesis, we have foamed constrained PMMA thin films generated at 40 °C and 34.5 MPa. In this series, the depressurization rate is varied (by the control valve assembly) from 0.345 to 6.89 MPa/s. As anticipated from CNT considerations, the highest cell nucleation densities coincide with the fastest depressurization rate explored (cf. Figure 11). The small population of large pore cells that results from

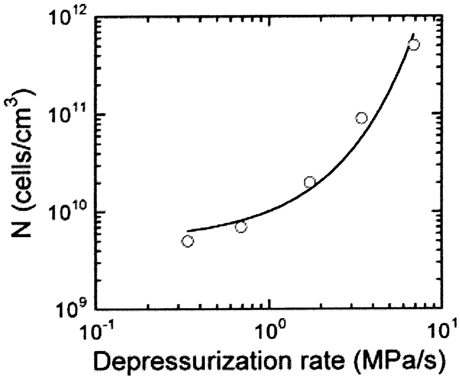

Figure 11. Dependence of cell density on depressurization rate at 40 °C and 34.5 MPa $scCO_2$ with surface constraints. The solid line, obtained by fitting a single exponential to the data, is provided as a guide for the eye.

slow depressurization reflects the increase in time over which depressurization proceeds. Although a large number of pore cells nucleate at the onset of foaming, an increase in depressurization time results in increased pore cell coalescence as CO_2 molecules from small cells merge into larger cells with lower overall surface area per unit volume. It follows that the depressurization time corresponds to the time available for the foam morphology to evolve from initial nucleation to the end of the growth period once the polymer vitrifies. Faster depressurization reduces this interval and prevents substantial coalescence prior to solidification.

Conclusions

In this study, we present a novel process strategy to produce tailored micro/mesocellular foams in PMMA thin films. This method restricts outward porogen diffusion to the film edges, thereby permitting retention of gas molecules for pore cell development even at relatively low saturation pressures and high foaming temperatures. While this work employs PMMA as the sole polymer to be foamed, the surface-constraint strategy developed here relies on fundamental transport principles and should extend to other polymers as well, which is demonstrated elsewhere.[41] The resultant foams not only exhibit uniform pore morphologies at submicron length scales but also possess thin unfoamed skins. An increase in cell density and a reduction in cell diameter are observed with increases in saturation pressure, exposure time, and depressurization rate, as well as with a decrease in temperature. Classical nucleation theory is modified to take into account the compressible nature of CO_2 and yields accurate predictions of cell nucleation density as a function of temperature and pressure. These results taken together demonstrate that constrained polymer foaming constitutes a promising and versatile route to the controllable production of novel and possibly nanostructured[42] polymeric materials.

Acknowledgment. This study was supported by the Kenan Center for the Utilization of Carbon Dioxide in Manufacturing and the STC Program of the National Science Foundation under Agreement CHE-9876674.

References and Notes

(1) Kazarian, S. G. *Polym. Sci., Ser. C* **2000**, *42*, 78.
(2) Tomasko, D. L.; Li, H. B.; Liu, D. H.; Han, X. M.; Wingert, M. J.; Lee, L. J.; Koelling, K. W. *Ind. Eng. Chem. Res.* **2003**, *42*, 6431. Tomasko, D. L.; Han, X. M.; Liu, D. H.; Gao, W. H. *Curr. Opin. Solid State Mater. Sci.* **2003**, *7*, 407.
(3) Cooper, A. I. *Adv. Mater.* **2003**, *15*, 1049.
(4) Eckert, C. A.; Knutson, B. L.; Debenedetti, P. G. *Nature (London)* **1996**, *383*, 313.
(5) Kirby, C. F.; McHugh, M. A. *Chem. Rev.* **1999**, *99*, 565.
(6) DeSimone, J. M. *Science* **2002**, *297*, 799.
(7) Park, C. B.; Suh, N. P. *Polym. Eng. Sci.* **1996**, *36*, 34.
(8) Siripurapu, S.; Gay, Y. J.; Royer, J. R.; DeSimone, J. M.; Spontak, R. J.; Khan, S. A. *Polymer* **2002**, *43*, 5511.
(9) Krause, B.; van der Vegt, N. F. A.; Wessling, M. *Desalination* **2002**, *144*, 5.
(10) Kumar, V.; Suh, N. P. *Polym. Eng. Sci.* **1990**, *30*, 1323.
(11) Goel, S. K.; Beckman, E. J. *Cell. Polym.* **1993**, *12*, 251.
(12) Arora, K. C.; Lesser, A. J.; McCarthy, T. J. *Macromolecules* **1998**, *31*, 4614.
(13) Stafford, C. M.; Russell, T. P.; McCarthy, T. J. *Macromolecules* **1999**, *32*, 7610.
(14) Krause, B.; Mettinkhof, R.; Vegt, N. F.; Wessling, M. *Macromolecules* **2001**, *34*, 874.
(15) Krause, B.; Sijbesma, H. J. P.; Munukulu, P.; Vegt, N. F.; Wessling, M. *Macromolecules* **2001**, *34*, 8792.
(16) Siripurapu, S.; DeSimone, J. M.; Khan, S. A.; Spontak, R. J. *Adv. Mater.* **2004**, *16*, 989.
(17) Baldwin, D. F.; Shimbo, M.; Suh, N. P. *J. Eng. Mater. Technol.—Trans. ASME* **1996**, *117*, 62.
(18) Martinache, J. D.; Royer, J. R.; Siripurapu, S.; Henon, F. E.; Genzer, J.; Khan, S. A.; Carbonell, R. G. *Ind. Eng. Chem. Res.* **2001**, *40*, 5570.
(19) Throne, J. L. *Thermoplastic Foams*; Sherwood Publishers: Hinckley, OH, 1996.
(20) Kumar, V., Weller, J. E., Eds.; *Polymeric Foams: Science and Technology*; American Chemical Society: Washington, DC, 1997.
(21) Klempner, D.; Sendijarevic, V. *Handbook of Polymeric Foams and Foams Technology*, 2nd ed.; Hanser: Munich, 2004.
(22) Huang, Q.; Seibig, B.; Paul, D. R. *J. Cell. Plast.* **2000**, *36*, 112.
(23) Howdle, S. M.; Watson, M. S.; Whitaker, M. J.; Popov, V. K.; Davies, M. C.; Mandel, F. S.; Wang, J. D.; Shakesheff, K. M. *Chem. Commun.* **2001**, 109.
(24) Yang, S.; Mirau, P. A.; Pai, C. S.; Nalamasu, O.; Reichmanis, E.; Pai, J. C.; Obeng, Y. S.; Seputro, J.; Lin, E. K.; Lee, H. J.; Sun, J. N.; Gidley, D. W. *Chem. Mater.* **2002**, *14*, 369.
(25) Saunier, J.; Alloin, F.; Sanchez, J. Y.; Barriere, B. *J. Polym. Sci., Part B: Polym. Phys.* **2004**, *42*, 532, 544.
(26) Barry, J. J. A.; Gidda, H. S.; Scotchford, C. A.; Howdle, S. M. *Biomater.* **2004**, *25*, 3559.
(27) Hedrick, J. L.; Miller, R. D.; Hawker, C. J.; Carter, K. R.; Volksen, W.; Yoon, D. Y.; Trollsås, M. *Adv. Mater.* **1998**, *10*, 1049. Hawker, C. J.; Hedrick, J. L.; Miller, R. D.; Volksen, W. *MRS Bull.* **2000**, *25*, 54. Hedrick, J. L.; Magbitang, T.; Connor, E. F.; Glauser, T.; Volksen, W.; Hawker, C. J.; Lee, V. Y.; Miller, R. D. *Chem.—Eur. J.* **2002**, *8*, 3308.
(28) Guarini, K. W.; Black, C. T.; Milkove, K. R.; Sandstorm, R. L. *J. Vac. Technol. B* **2001**, *19*, 2784.
(29) Soler-Illia, G. J. D. A.; Crepaldi, E. L.; Grosso, D.; Sanchez, C. *Curr. Opin. Colloid Interface Sci.* **2003**, *8*, 109.
(30) Krause, B.; Koops, G.-H.; van der Vegt, N. F. A.; Wessling, M.; Wübbenhorst, M.; van Turnhout, J. *Adv. Mater.* **2002**, *14*, 1041.
(31) Imhof, A.; Pine, D. J. *Nature (London)* **1997**, *389*, 948.
(32) Walheim, S.; Schaffer, E.; Mlynek, J.; Steiner, U. *Science* **1999**, *283*, 520.
(33) Krause, B.; Diekmann, K.; Vegt, N. F. A.; Wessling, M. *Macromolecules* **2002**, *35*, 1738.
(34) Colton, J. S.; Suh, N. P. *Polym. Eng. Sci.* **1987**, *27*, 485, 493, 500.
(35) Shafi, M. A.; Flumermelt, R. W. *Chem. Eng. Sci.* **1997**, *52*, 627. Shafi, M. A.; Joshi, K.; Flumermelt, R. W. *Chem. Eng. Sci.* **1997**, *52*, 635.
(36) Goel, S. K.; Beckman, E. J. *Polym. Eng. Sci.* **1994**, *34*, 1137, 1148.
(37) See, for example: Nishioka, K.; Kusaka, I. *J. Chem. Phys.* **1992**, *96*, 5370. Müller, M.; MacDowell, L. G.; Virnau, P.; Binder, K. *J. Chem. Phys.* **2002**, *117*, 5480. Feng, J. J.; Bertelo, C. A. *J. Rheol.* **2004**, *48*, 439.
(38) Harrison, K. L.; Johnston, K. P.; Sanchez, I. C. *Langmuir* **1996**, *12*, 2637.

(39) Sanchez, I. C.; Lacombe, R. H. *J. Phys. Chem.* **1976**, *80*, 2352. Lacombe, R. H.; Sanchez, I. C. *J. Phys. Chem.* **1976**, *80*, 2558. Sanchez, I. C.; Lacombe, R. H. *Macromolecules* **1978**, *11*, 1145.

(40) Royer, J. R.; De Simone, J. M.; Khan, S. A. *Macromolecules* **1999**, *32*, 8965. Walker, T. A.; Colina, C. M.; Gubbins, K. E.; Spontak, R. J. *Macromolecules* **2004**, *37*, 2588.

(41) Frankowski, D. J.; Fournier-Bidoz, S.; Manners, I.; Ozin, G. A.; Khan, S. A.; Spontak, R. J. *Macromol. Chem. Phys.* **2004**, *205*, 2398.

(42) Frankowski, D. J.; Raez, J.; Manners, I.; Winnik, M. A.; Khan, S. A.; Spontak, R. J. *Langmuir* **2004**, *20*, 9304.

MA0484983